This is a repository copy of *Hybrid Reluctance Machine with Skewed Permanent Magnets and Zero-Sequence Current Excitation*.

White Rose Research Online URL for this paper:
https://eprints.whiterose.ac.uk/id/eprint/195693/

Version: Published Version

*Article*

# Hybrid Reluctance Machine with Skewed Permanent Magnets and Zero-Sequence Current Excitation

**Ziqi Huang [1]**, **Xing Zhao [2]**, **Weiyu Wang [1]** and **Shuangxia Niu [1,*]**

1   Department of Electrical Engineering, The Hong Kong Polytechnic University, Hong Kong, China
2   Department of Electronic Engineering, The University of York, York YO10 5DD, UK
*   Correspondence: eesxniu@polyu.edu.hk

**Abstract:** The reluctance machine is a potential candidate for electrical vehicle propulsion because of its reliable structure, low cost, flexible flux regulation ability, and wide speed range. However, the torque density is unsatisfactory because of the poor excitation ability and low stator core utilization factor. To solve this problem, in this paper, a novel hybrid reluctance machine (HRM) with the skewed permanent magnet (PM) and the zero-sequence current is proposed for electric vehicles. The skewed PM has two magnetomotive force (MMF) components with different functions. The radial MMF component provides extra torque by the flux modulation effect. The tangential MMF component can generate a constant biased field in the stator core to relieve the saturation caused by the zero-sequence current and thus improve the utilization factor of the stator core. Therefore, torque improvement and the relief of stator core saturation can be simultaneously achieved by the skewed PM. In this paper, the machine structure and principle of the proposed machine are introduced. And ultimately, the machine's electromagnetic performances are evaluated under different PM magnetization directions and zero-sequence current angles by using finite element analysis (FEA).

**Keywords:** finite element methods; permanent magnet; reluctance machines

## 1. Introduction

With the growing concern regarding global warming, energy shortages, and pollutant emission, there is a worldwide tendency to use electric vehicles (EV) and hybrid electric vehicles (HEV) to replace traditional internal combustion engine vehicles. The electric machine, as the key component in EV and HEV propulsion systems, is required to have high efficiency, high torque/power density, and a wide speed range [1–4]. There are mainly three main types of machines that are candidates for the excitation source, namely, PM-excited, DC-excited, and hybrid excited machines.

PM-excited machines usually have higher torque production than DC-excited machines because the excitation ability of DC current is lower than that of the PM with a limited slot area and heat dissipation condition [5,6]. High efficiency is also a merit of PM-excited machines because PMs can produce a magnetic field without any input energy [7]. However, the PM machines face some drawbacks, such as their poor flux regulation ability and resultant smaller speed range, due to the fixed PM flux [8]. In addition, the risk of demagnetization and the high price of PM materials limit the application of PM-excited machines [9]. Some trade-offs must be involved to balance the PM-excitation and DC excitation, and therefore hybrid excited machines have become an emerging solution for EV applications.

Hybrid excited machines can be classified into two types according to the location of the PM material (rotor side or stator side). Machines with stator PMs have attracted more research attention in recent decades because of the definite advantages of their robust structure, high power density, and high efficiency [10]. The PM material is designed on the stator side so that it does not suffer from the effect of centrifugal force. The rotor usually

consists of an iron core only and thus enjoys higher robustness so that a higher rotor speed can be applied [11]. Among the hybrid excited machines with stator PMs, the switched reluctance machine (SRM) is a promising potential solution [9]. The most attractive point of the SRM is its simple and robust structure, as the rotor consists of an iron core only, and all winding and PM are designed on the stator [12]. Compared with the original DC-excited SRM from 1839 [13], the latter hybrid excited SRMs employ PMs in the machine, and the torque production and efficiency are improved.

In general, according to the magnetic circuit topology, there are two main types of hybrid excited SRM, namely, the parallel-excited type and the series-excited type. For series-excited hybrid SRMs, although the torque is directly promoted because of the extra field source from the PM, the high magnetic resistance constrains the field adjustment ability of the DC coil. Additionally, the PM material faces a higher demagnetization risk when the reversed DC current is applied at the flux-weakening region [14,15]. By contrast, the PM material faces less demagnetization risk in the parallel-excited SRMs, and therefore, it has attracted more research interest.

In recent years, various parallel-excited SRMs have been investigated [16–27]. The PM material is usually assigned at the slot opening so that the stator core would not be separated, and a low-order working harmonic can be utilized because the slot opening PM does not change the reluctance of the stator core in the magnetic circuit. These machines have similar configurations but different working principles and torque performance. In [16], under the flux modulation effect, a hybrid-excited reluctance machine with the radial magnetized PM is proposed. Under the flux modulation effect, although the DC current and the PM have different main working harmonic orders, both of them can be utilized by a concentrated winding configuration. However, the stator suffers from easy saturation because the BH working range is limited within the first quadrant. In [17–19], the parallel-excited PM is arranged with an opposite magnetization direction to the DC current to expand the BH working range. In this way, the stator core utilization factor is improved, and torque production is raised. However, the current is not sinusoidal, and the torque ripple is still very high because of its half-cycle-conducting operation principle. To address this issue, another alternate solution utilizing the flux modulation principle is proposed in [20], where the sinusoidal current is applied, and the torque ripple is largely reduced. The DC-saturation-relieving effect also extends the BH working range of the stator core so that the relatively higher DC current can be applied. Based on this idea, various hybrid-excited reluctance machines with tangential magnetized PMs have been proposed, where the DC current can produce working air-gap harmonics under the flux modulation effect, while the tangential magnetized PM can relieve the saturation of the stator core [21–23]. However, the PM cannot provide an effective flux directly, and therefore torque production is still unsatisfactory. In [24], a synthetic PM structure is outlined in which a group of tangential magnetized PMs and the radial magnetized PM are used for saturation relief and torque improvement, respectively. However, this PM structure is quite complicated, and therefore, in [25], the skewed PM is used to replace the synthetic PM. However, one concern for this type of machine is yet to be solved, namely the conflict with the AC winding in the stator slot area caused by the introduction of the DC winding. AC armature winding with the zero-sequence current is a possible solution, as here AC and DC coils are combined, which reduces the copper loss under the same ampere-turn number and increases the efficiency [26].

To give consideration to both torque production and flux regulation ability in hybrid excited HRMs, this paper adopts the skewed PM to improve the torque production with the flux modulation effect and to promote flux regulation ability and reliving-DC-saturation relief simultaneously. In addition, the AC and DC windings were combined, and the zero-sequence current was adopted as a torque generation source. This paper is organized as follows. In Section 2, the machine structure and the working principle of the proposed machine are presented. In Section 3, the electromagnetic performances are evaluated to give design instructions for the proposed machine, especially as concerns the magnetization

direction of the skewed PM and the zero-sequence current ratio. In Section 4, some conclusions are provided.

## 2. Machine Structure and Operation Principle

### 2.1. Machine Structure

The structure of the proposed hybrid reluctance machine (HRM) is presented in Figure 1. The rotor consists of iron core only, thus having good mechanical robustness. The skewed PMs located at slot openings have two magnetization components. One component is tangentially magnetized with alternate polarity in every adjacent PM. The other component is radial magnetized and all PMs are outwards magnetized. In spite of the slightly higher complexity of manufacturing of skewed PM than traditional PM, it is acceptable due to the good electromagnetic performance of the proposed machine. There are two groups of 3-phase winding, which are shown in Figure 2. The neutral points of two winding groups are connected, which provides a path for zero-sequence current. The current in all windings can be illustrated as:

$$\begin{cases} I_{A1} = \sqrt{2}I_{ac}sin(\omega t + \varphi_0) + I_0 \\ I_{B1} = \sqrt{2}I_{ac}sin(\omega t + \varphi_0 - 120°) + I_0 \\ I_{C1} = \sqrt{2}I_{ac}sin(\omega t + \varphi_0 + 120°) + I_0 \\ I_{A2} = \sqrt{2}I_{ac}sin(\omega t + \varphi_0) - I_0 \\ I_{B2} = \sqrt{2}I_{ac}sin(\omega t + \varphi_0 - 120°) - I_0 \\ I_{C2} = \sqrt{2}I_{ac}sin(\omega t + \varphi_0 + 120°) - I_0 \end{cases} \quad (1)$$

where $I_{A1}$, $I_{B1}$, $I_{C1}$, $I_{A2}$, $I_{B2}$, and $I_{C2}$ represent the phase current in phase A1, B1, C1, A2, B2, and C2 respectively. $I_{ac}$ and $I_0$ are the AC and zero-sequence components of phase current. $\omega$ and $\varphi_0$ are the electric rotation speed and initial position. As all excitation sources (PM and winding current) are assigned at the stator side, the proposed machine enjoys good cooling properties compared with traditional rotor-PM machines [27–30]. Furthermore, by replacing the AC and DC coils with integrated winding, the copper loss can be reduced under the equivalent magnetomotive force (MMF) produced by the current.
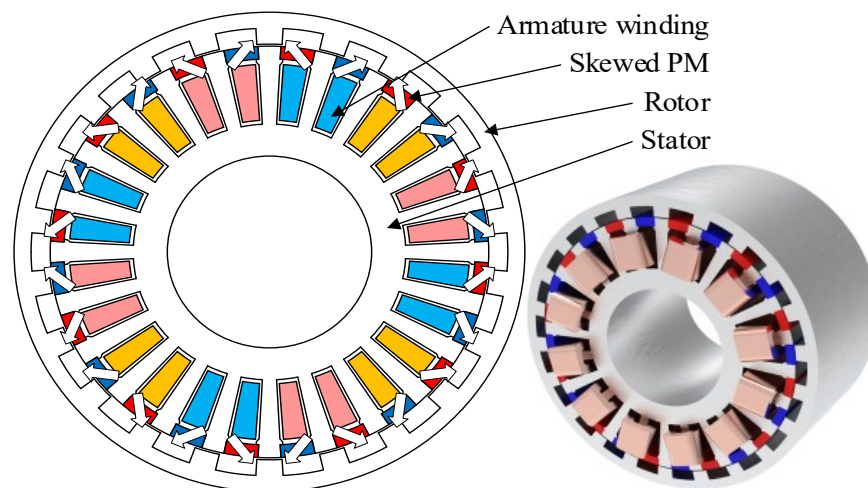


**Figure 1.** Structure of hybrid reluctance machine with skewed PM.

As is presented in Figure 3, the MMF of the skewed PM has two components, including radial ($F_{PMr}$) and tangential ($F_{PMt}$) components. The working principle of $F_{PMt}$ and its associated DC-saturation-relieving effect is introduced in the next part. The working principle of $F_{PMr}$ and its associated flux modulation effect is presented in the last part of this section.
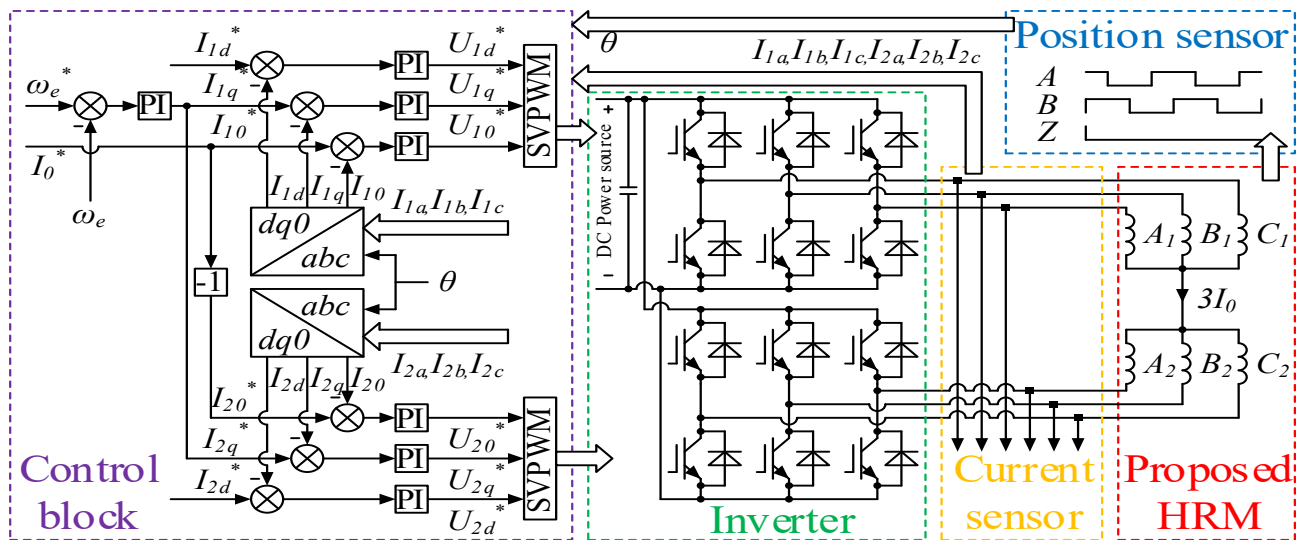
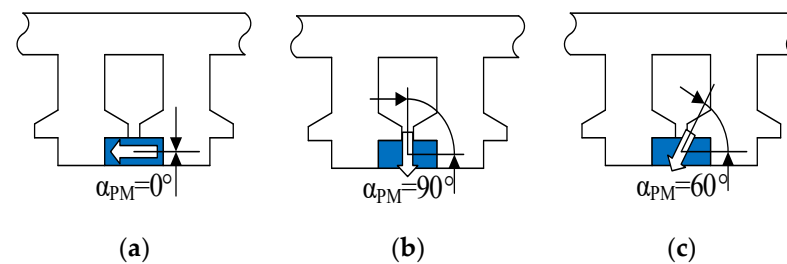**Figure 2.** Winding configuration and control circuit.



**Figure 3.** PMs with different $\alpha_{PM}$. (**a**) PM with only $F_{PMt}$. (**b**) PM with only $F_{PMr}$. (**c**) proposed PM design with both $F_{PMt}$ and $F_{PMr}$.

### 2.2. $F_{PMt}$ and DC-Saturation-Relieving Effect

This part shows the working principle of the tangential component of the MMF of the skewed PM ($F_{PMt}$) and its associated DC-saturation-relieving effect with $I_0$.

To give an intuitive illustration, the flux paths of $F_{PMt}$ and $I_0$ are presented in Figure 4, where $\Phi_{PMt}$ and $\Phi_0$ are the fields from $F_{PMt}$ and $I_0$, respectively. When the rotor is at position A/B, the rotor permeance is at max/min value, and thus $\Phi_0$ is at max/min value. If $\Phi_{PMt}$ is not used, the BH vibration range of $\Phi_0$ is limited within the first quadrant, which causes a low utilization factor of the stator core. To overcome this problem, $\Phi_{PMt}$ provided a constant biased flux with opposite polarity with $\Phi_0$. However, $\Phi_{PMt}$ produces little effective back EMF in the armature winding directly because it is short-circuited in the magnetic circuit. The BH working range can be shifted to another quadrant as shown in Figure 5 from ΔB1 to ΔB2 with $F_{PMt}$. As a result, the stator core can be better utilized, higher $I_0$ can be applied, and therefore, a wider voltage regulation range (VRR) can be achieved.
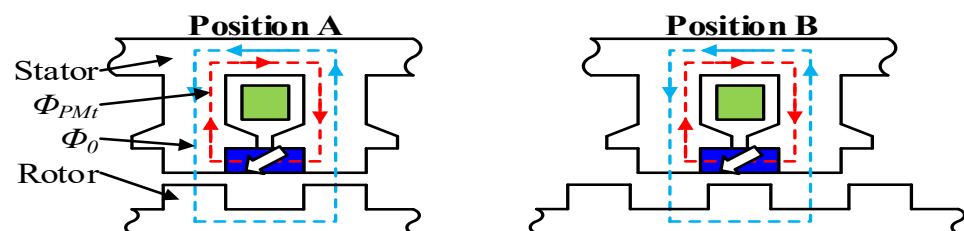


**Figure 4.** Flux path of the tangential component of the skewed PM and DC current.
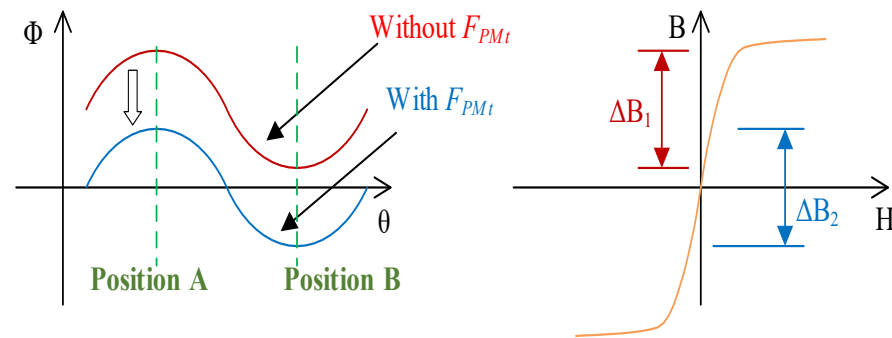
**Figure 5.** Schematic flux waveform in the stator tooth and BH working range.

To provide a quantitative analysis of $\Phi_{PMt}$, the equivalent magnetic circuit is presented in Figure 6, where $F_0$ is the equivalent MMF of $I_0$. And $R_r$, $R_y$, $R_t$, $R_{PMt}$, and $R_g$ are the reluctances of the rotor yoke, stator yoke, stator tooth, PM, and air gap, respectively.

$$\begin{bmatrix} 0 & -R_{PMt} & R_g & R_1 \\ -R_{PMt} & 0 & R_1 & R_g \\ R_t & R_1 & 0 & -R_{PMt} \\ R_1 & R_t & -R_{PMt} & 0 \end{bmatrix} \begin{bmatrix} \Phi_{s1} \\ \Phi_{s2} \\ \Phi_{r1} \\ \Phi_{r2} \end{bmatrix} = \begin{bmatrix} F_{PMt} \\ F_{PMt} \\ F_0 - F_{PMt} \\ F_0 - F_{PMt} \end{bmatrix} \quad (2)$$

$$\begin{cases} F_{PMt} = H_c L_{PMt} cos\alpha_{PM} \\ F_0 = N_t I_0 \\ R_1 = R_{PMt} + 2R_g + R_r \end{cases} \quad (3)$$



**(a)**           **(b)**
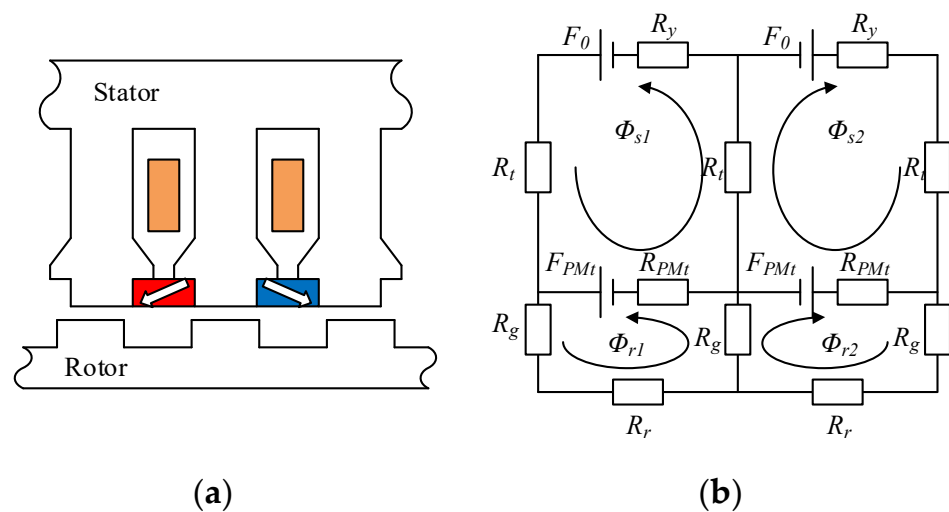
**Figure 6.** The no-load magnetic circuit of the proposed machine. (**a**) proposed machine (**b**) the no-load magnetic circuit.

Based on the magnetic circuit, the no-load flux can be expressed in (2) and (3), where $H_c$ is the coercive force of the PM, $L_{PMt}$ is the tangential length of the PM, $N_t$ is the number of the turns of armature winding, and $\alpha_{PM}$ is the magnetization direction of PM. Therefore, the flux in stator tooth ($\Phi_{st}$) can be presented as:

$$\Phi_{st} = \Phi_{s1} + \Phi_{s2} = \left( \frac{2}{R_2} + \frac{2R_{PMt}}{R_2(R_r + 3R_g)} \right) F_0 - \frac{2}{R_2} F_{PMt} \quad (4)$$

where $R_2 = \left( \frac{2}{R_2} + \frac{2R_{PMt}}{R_2(R_r+3R_g)} \right) F_0 - \frac{2}{R_2} F_{PMt}$.

It is validated in (4) that the flux from $F_0$ and $F_{PMt}$ have opposite directions because the first term is always positive, while the second term is always negative. Both terms are relevant to $R_g$, which depends on the rotor position. Therefore, both $F_0$ and $F_{PMt}$ can contribute to back EMF and torque generation. However, the reluctance of the stator yoke ($R_y$) and tooth ($R_t$) is very small compared with $R_{PMt}$. If $R_y$ and $R_t$ are neglected, $R_2$ is approximately equal to $R_{PMt}$. Therefore, (4) can be rewritten as:

$$\Phi_{st} \approx \left( \frac{2}{R_{PMt}} + \frac{2}{R_r + 3R_g} \right) F_0 - \frac{2}{R_{PMt}} F_{PMt} \tag{5}$$

As is presented in (5), the flux from $F_{PMt}$ is independent of $R_g$ if $R_y$ and $R_t$ are neglected. It implies that $F_{PMt}$ only provides a constant biased flux in the stator core to relieve the saturation. While $F_0$ is still relevant to $R_g$ in (5), which proves that it can contribute to torque generation. When designing the skewed PM, the maximum and minimum value of $\Phi_{st}$ should satisfy (6) to fully utilize the stator core.

$$\Phi_{st.mean} = \frac{\Phi_{st.max} + \Phi_{st.min}}{2} = 0 \tag{6}$$

By combining (3) and (5) with (6), we can obtain:

$$N_t I_0 \left( 1 + \frac{R_{PMt}}{2R_{r.max} + 6R_g} + \frac{R_{PMt}}{2R_{r.min} + 6R_g} \right) - H_c L_{PMt} cos\alpha_{PM} = 0 \tag{7}$$

Equation (7) gives analytical instructions for designing $\alpha_{PM}$. If $\alpha_{PM}$ is too high, $\Phi_{st.mean}$ will still be positive, and the stator tooth will be under-relieved. If $\alpha_{PM}$ is too low, $\Phi_{st.mean}$ will become negative, which means the stator tooth will be over-relieved. Both under-relieved and over-relieved limit torque production. The detailed analysis for the appropriate value of $\alpha_{PM}$ with FEA results is presented in Section 3.

### 2.3. $F_{PMr}$ and Flux Modulation Effect

This part shows the working principle of $F_{PMr}$ and the associated flux modulation effect. $F_{PMr}$ produces an effective back EMF in the armature winding directly. As the radial magnetization component of the skewed PM is outwards for all PMs, the associated air gap MMF can be expressed in Figures 7 and 8, while the air gap permeance of the rotor ($P_r(\theta,t)$) can be expressed as shown in Figures 8 and 9.

$$\begin{cases} F_r(\theta) = \sum_{n=1}^{+\infty} F_n cos(nN_{slot}\theta) \\ F_n = \frac{2}{n\pi} F_{PMr} sin\left( nN_{slot} \frac{\theta_{PM}}{2} \right) \\ F_{PMr} = H_c L_{PMr} sin\alpha_{PM} \end{cases} \tag{8}$$

$$\begin{cases} P_r(\theta, t) = \frac{P_0}{2} + \sum_{k=1}^{+\infty} P_k cos[kN_r(\theta - \omega_{me}t)] \\ P_0 = 2P_2 + \frac{(P_1 - P_2)}{\pi} \theta_{rt} N_r \\ P_k = \frac{2}{k\pi} (P_1 - P_2) sin\left( nN_r \frac{\theta_{rt}}{2} \right) \end{cases} \tag{9}$$

where $F_r(\theta)$ is the air gap MMF of the radial component of the skewed PM, $\theta$ is the mechanical angle, $N_{slot}$ is the slot number, $\theta_{PM}$ is the PM central angle, $F_{PMr}$ is the equivalent MMF of the radial component of the skewed PM, and $L_{PMr}$ is the radial length of skewed PM. $P_1$ is the permeance of the rotor salient poles, $P_2$ is the permeance of rotor slots, $N_r$ is

the number of the rotor salient poles, $\omega_{me}$ is the mechanical angular speed of the rotor, $\theta_{rt}$ is the mechanical angle of the rotor tooth. The air gap flux density can be calculated as:

$$B_{PMr}(\theta,t) = F_r(\theta)P_r(\theta,t) = \sum_{n=-\infty}^{+\infty}\sum_{k=1}^{+\infty}\frac{F_n P_k}{2}cos[(kN_r + nN_{slot})\theta - kN_r\omega_{me}t] \quad (10)$$
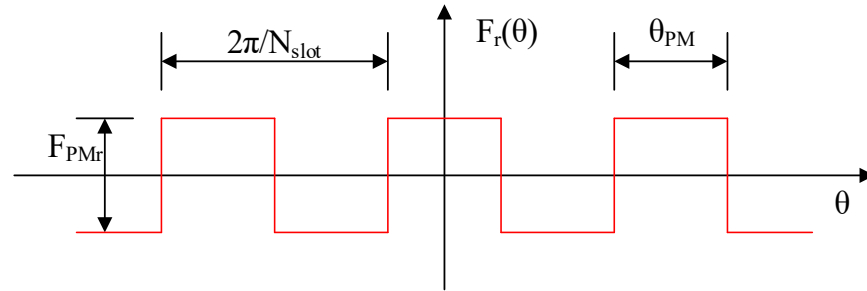


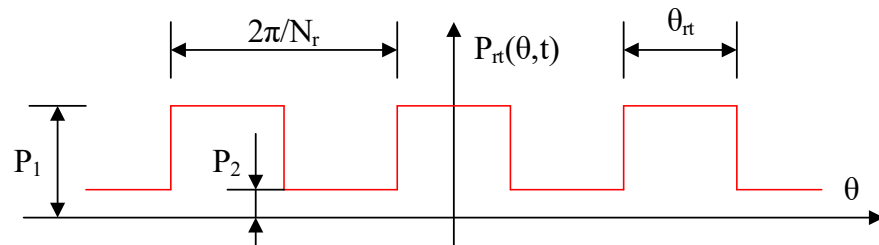**Figure 7.** Air gap MMF of the radial component of the skewed PM.



**Figure 8.** Air gap permeance of the rotor.

According to (10), the harmonic order of air gap flux density and corresponding rotation speed can be expressed as:

$$\begin{cases} P_{(n,k)} &= |kN_r + nN_{slot}| \\ \omega_{(n,k)} &= \left|\frac{kN_r\omega_{me}}{kN_r + nN_{slot}}\right| \end{cases}, n = 0, \pm1, \pm2, \ldots, k = 1, 2, 3, \ldots. \quad (11)$$

According to the flux modulation effect, the main working harmonic corresponds to the case in which $k = 1$ and $n = -1$. Therefore, the order of the main working harmonic of the radial component of the skewed PM satisfies (12).

$$P_{aw} = |N_r - N_{slot}| \quad (12)$$

where $P_{aw}$, $N_{slot}$, and $N_r$ are the pole pair numbers of the armature winding, slot number, and rotor pole number, respectively.

For the main working harmonic of the radial component of the skewed PM, the torque contribution is in direct proportion to the back EMF if saturation is not considered. The back EMF contributed by the main working harmonic is expressed as:

$$\begin{cases} E_{phn} &= \frac{4.44 D_o L_s N_t}{60} B_{(n,k)} k_{wn}\omega_{(n,k)} \\ B_{(-1,1)} &= \frac{2H_c L_{PMr}(P_1 - P_2)}{\pi^2}sin\left(\frac{N_{slot}\theta_{PM}}{2}\right)sin\left(\frac{N_r\theta_{rt}}{2}\right)sin\alpha_{PM} \end{cases} \quad (13)$$

where $E_{phn}$ is the back EMF of the nth harmonic, $B_{(n,k)}$ is the corresponding harmonic amplitude, $k_{wn}$ is the winding factor, $D_o$ is the circumferential diameter of the air gap, and $L_s$ is the stack length [31]. It is implied in (13) that the back EMF contributed by the main working harmonic is in direct proportion to $sin(\alpha_{PM})$. The higher $\alpha_{PM}$ is, the higher the back EMF and associated higher torque production.

## 3. Electromagnetic Performance

This part evaluates the electromagnetic performance of the proposed machine. Firstly, the analysis of the three essential design parameters is presented, namely the PM magnetization direction ($\alpha_{PM}$), the zero-sequence current ratio ($\alpha$), and the current angle ($\beta$), which are presented in Figure 9. The following FEA results are based on the dimensional data in Table 1 and Figure 10.

**Table 1.** Design Parameters of the HRM with Skewed PM.

| Item | Unit | Notation | Value |
|------|------|----------|-------|
| Outer radius | mm | $R_o$ | 75 |
| Stack length | mm | $L_s$ | 80 |
| Rotor yoke thickness | mm | $T_{ry}$ | 5 |
| Rotor tooth height | mm | $H_{rt}$ | 5 |
| Rotor tooth central angle | deg | $\theta_{rt}$ | 6.55 |
| Air gap length | mm | $g$ | 0.5 |
| PM magnetization angle | deg | $\alpha_{PM}$ | 60 |
| PM central angle | deg | $\theta_{PM}$ | 9 |
| PM height | mm | $H_{PM}$ | 4 |
| Pole shoe height | mm | $H_s$ | 1 |
| Stator yoke thickness | mm | $T_{sy}$ | 10 |
| Stator tooth central angle | deg | $\theta_{st}$ | 6 |
| Inner radius | mm | $R_i$ | 30 |
| Estimated slot filling factor | / | $k_{sf}$ | 0.7 |
| Rated current density | A/mm$^2$ | $D$ | 6 |
| Rated speed | rpm | $S_{pd}$ | 600 |
| Coil turns | / | $N_t$ | 105 |
| AC component of armature current | A | $I_{ac}$ | 5.35 |
| Zero-sequence current | A | $I_0$ | 2.72 |
| Stator slot number | / | $N_{slot}$ | 24 |
| Rotor pole number | / | $N_r$ | 22 |
| Winding pole pair number | / | $P_{aw}$ | 2 |
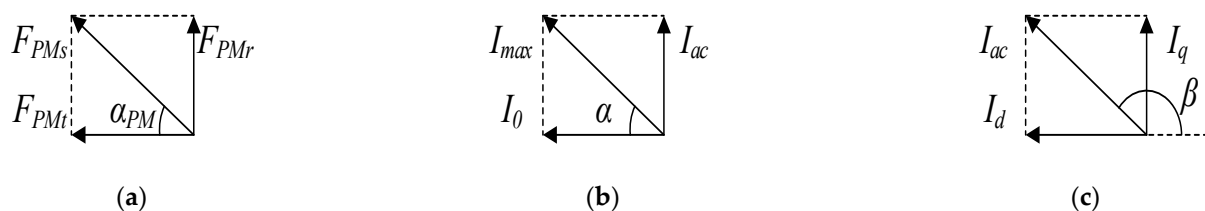


**Figure 9.** Schematic explanation. (**a**) PM magnetization direction $\alpha_{PM}$. (**b**) zero-sequence current ratio $\alpha$. (**c**) current angle $\beta$.
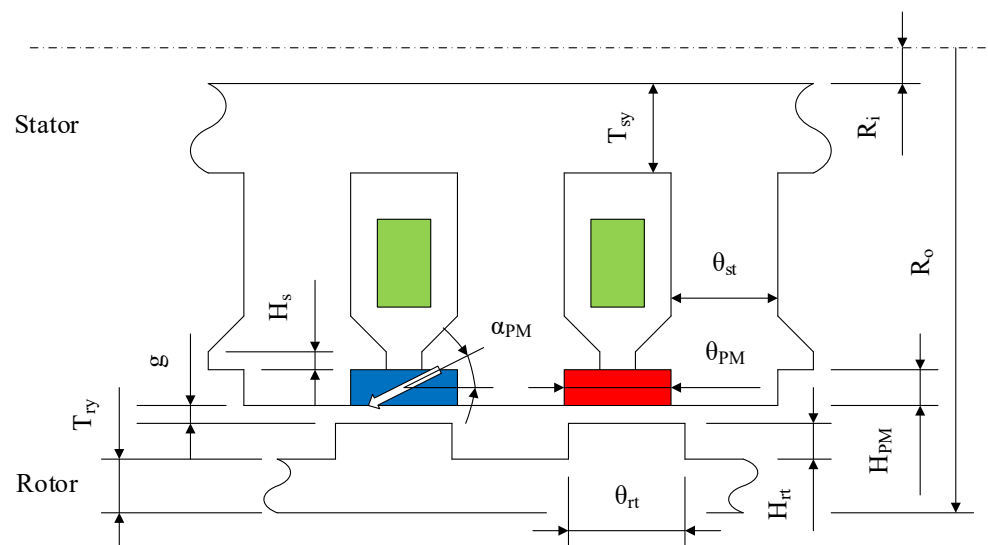
**Figure 10.** Notations of dimensional parameters.

### 3.1. Magnetization Direction

This part gives a detailed evaluation of the magnetization direction of the skewed PM ($\alpha_{PM}$) in terms of the flux density vibration range, no-load back EMF, voltage regulation rate (VRR), and torque production.

As was explained in the last Section, the purpose of $F_{PMr}$ is to provide an additional excitation source, which can improve the back EMF and associated torque promotion directly. The purpose of $F_{PMt}$ is to provide a constant biased flux to relieve the saturation in the stator core so that the stator core utilization factor can be improved and the flux regulation ability can be promoted. Therefore, a trade-off between two magnetization components must be considered.

Figure 11 shows the vibration range of the no-load flux density in the stator tooth and the associated back EMF with different $\alpha_{PM}$. $B_{max}$ and $B_{min}$ are the maximum and minimum values of flux density. $E_{63°}$ is the back EMF when $\alpha$ is set at 63°.



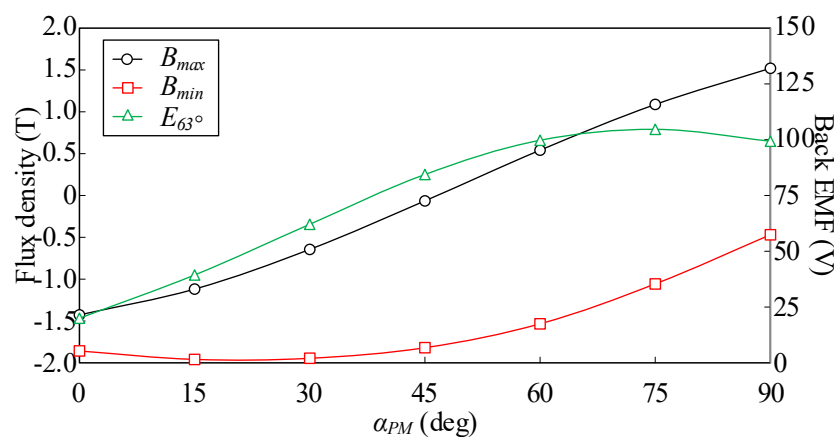**Figure 11.** No−load vibration range of flux density in stator tooth and associated back EMF in the armature winding with different αPM.

When $\alpha_{PM}$ is at 0°, the skewed PM has only the MMF tangential component, the flux of which is much stronger than that of the zero-sequence current. Therefore, the stator core is over-relieved. When $\alpha_{PM}$ is increased, the tangential component of PM is reduced, and therefore, the vibration range of the flux density moves up. In addition, the associated back EMF is also promoted because of the introduction of $F_{PMr}$. However, at the high $\alpha_{PM}$

region, the flux from $F_{PMt}$ is too weak to relieve the saturation, which causes saturation and an associated drop in the amplitude of the back EMF.

The voltage regulation rate (VRR) is also a key concern when designing the proposed machine. It represents the voltage regulation ability of $I_0$, and therefore, it largely determines the speed range at the flux weakening region. In this paper, the VRR is defined as:

$$VRR = \frac{E_{0°} - E_{90°}}{E_{45°}} \tag{14}$$

where $E_{0°}$, $E_{45°}$, and $E_{90°}$ represent the back EMF with $\alpha$ of $0°$, $45°$, and $90°$, respectively. The VRR with different $\alpha_{PM}$ are evaluated and presented in Figure 12. The lower $\alpha_{PM}$ is, the higher the VRR that can be achieved. The average torque, another key concern for design, is also evaluated in Figure 12. The highest average torque can be achieved when $\alpha_{PM}$ is at roughly $60°$, which basically agrees with the waveform of the back EMF.
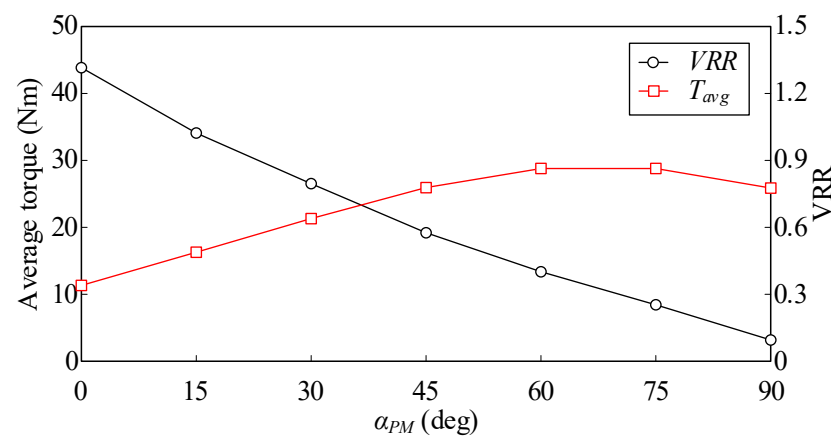


**Figure 12.** Average torque and VRR with different PM magnetization directions.

To give a deeper understanding of the principle of the skewed PM, a more intuitive explanation for the torque increase due to this optimal magnetization angle is provided below.

The purpose of the radial component of the MMF of the skewed PM ($F_{PMr}$) is to provide an additional excitation source for the proposed machine. Therefore, the higher $F_{PMr}$ is, the higher the torque contribution that can be achieved if the core saturation is ignored. However, in a hybrid-excited machine, the zero-sequence current in the armature winding may cause severe saturation, especially at high current conditions, which further limits the torque production of the proposed machine. Therefore, the tangential component of MMF of skewed PM ($F_{PMt}$) is used to relieve the core saturation. The higher the zero-sequence current is, the higher $F_{PMt}$ is required. In this paper, the current density is set to 6 A/mm². Therefore, the corresponding $\alpha_{PM}$ is set to 60 deg.

### 3.2. Zero-Sequence Current Ratio and Current Angle

In the proposed machine, the copper loss can be reduced when zero-sequence current is used to replace the traditional DC and AC winding design. The reason is presented below.

In the traditional design, the total copper loss ($P_{trad}$) can be expressed as:

$$P_{trad} = P_{ac} + P_{dc} = I_{ac}^2 R_{ac} + I_{dc}^2 R_{dc} \tag{15}$$

$$\begin{cases} I_{ac} = \frac{k_{ac} S_{total} k_{sf} D}{N_{ac}}, R_{ac} = \frac{L_{ac} N_{ac}^2}{\sigma S_{ac} k_{sf}}, k_{ac} = \frac{S_{ac}}{S_{total}} \\ I_{dc} = \frac{k_{dc} S_{total} k_{sf} D}{N_{dc}}, R_{dc} = \frac{L_{dc} N_{dc}^2}{\sigma S_{dc} k_{sf}}, k_{dc} = \frac{S_{dc}}{S_{total}} \end{cases} \tag{16}$$

where $P_{ac}$ and $P_{dc}$ are the copper loss, $I_{ac}$ and $I_{dc}$ are the current value, $R_{ac}$ and $R_{dc}$ are the winding resistance, $S_{ac}$ and $S_{dc}$ are the slot area that each coil takes up, $L_{dc}$ and $L_{ac}$ are the coil length per turn, $N_{dc}$ and $N_{ac}$ are the number of turns of the AC/DC coils, $k_{sf}$ is the slot

filling factor, $\sigma$ is the conductivity of copper, and $S_{total}$ is the total slot area. In this machine, AC and DC coils have the same length per turn because the concentrated winding is used for both AC and DC coils.

$$L_{ac} = L_{dc} = L \tag{17}$$

By combining (16) and (17) with (15), we can obtain:

$$P_{trad} = \frac{S_{total}k_{sf}D^2L}{\sigma} \tag{18}$$

By contrast, under the same current excitation, when the zero-sequence current is used to replace the original AC/DC coils, the total copper loss ($P_{prop}$) can be expressed as:

$$P_{prop} = \left(I_{ac}^2 + I_{dc}^2\right)\frac{LN_t^2}{\sigma S_{total}k_{sf}} \tag{19}$$

where $N_t$ is the number of turns. By combining (16) and (19), we can obtain:

$$P_{prop} = \frac{S_{total}k_{sf}D^2L}{\sigma}\left(k_{dc}^2 + k_{ac}^2\right) \tag{20}$$

From comparing (18) with (20), it is obvious that $P_{prop}$ is always smaller than $P_{trad}$. The following part investigates the influence that $\alpha$ and $\beta$ have on machine performance. According to the results of the previous part, the highest $T_{avg}$ can be achieved at $\alpha_{PM} = 60°$. Thus, in this part, $\alpha_{PM}$ is set to $60°$.

Figure 13a shows the average torque with different $\alpha$ values when $\beta$ is $90°$. When $\alpha$ is $0°$, $I_0$ attains its maximum value. However, there is no AC component in the phase current, and therefore, no torque production can be obtained. With a low $\alpha$ region (roughly $0°$ to $30°$), the average torque is almost in direct proportion to $\alpha$. However, the increments reduce as $\alpha$ grows because the excitation field from $I_0$ is reduced. The torque even drops at the high $\alpha$ region because the excitation field from $I_0$ is too low. Considering the trade-off between $I_0$ and $I_{ac}$, the maximum torque can be obtained when $\alpha = 63°$.
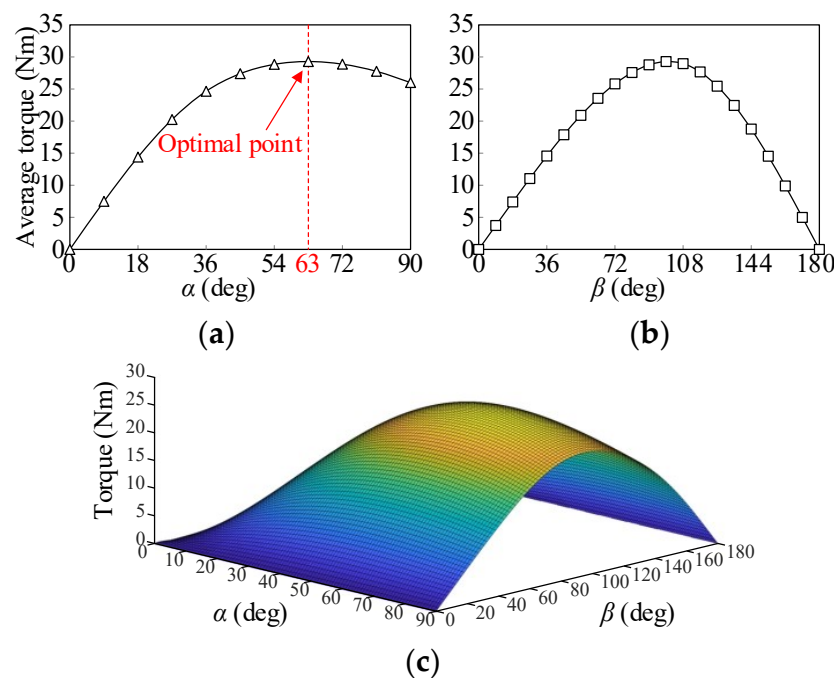


**Figure 13.** Torque production under different $\alpha$ and $\beta$ values when $\alpha$PM = 60°. (**a**) when $\beta$ = 90°. (**b**) when $\alpha$ = 63°. (**c**) overall results.

Figure 13b shows the torque production with different $\beta$ when $\alpha$ is 63°. It can be seen that the curve is close to the sinusoid. This is because the machine can be approximately seen as a non-salient pole machine when the fluctuation of the winding inductance against the rotor position is small due to the specially selected slot/pole combination. The torque production at the maximum torque per ampere (MTPA) point is very close to that of $\beta = 90°$. Therefore, the traditional $i_d = 0$ control for synchronous machines can be directly applied.

### 3.3. Magnetic Flux Distribution

This part provides an analysis of the no-load flux distributions under different excitation sources. Figure 14 shows the flux modulation effect, while Figure 15 shows the DC-saturation-relieving effect. In this example case, $N_r = 22$ and $N_{slot} = 24$. Under the flux modulation effect, it is clear that a two-pole-pair flux is built in Figure 14, which agrees with (12). Figure 15a shows the flux from $I_0$, which is biased and opposite to that of $\Phi_{PMt}$ shown in Figure 15b. In Figure 15c, it can be observed that the flux density in the stator core is largely relieved when $\Phi_{PMt}$ is used together with $\Phi_0$, which proves the effectiveness of the DC-saturation-relieving effect.
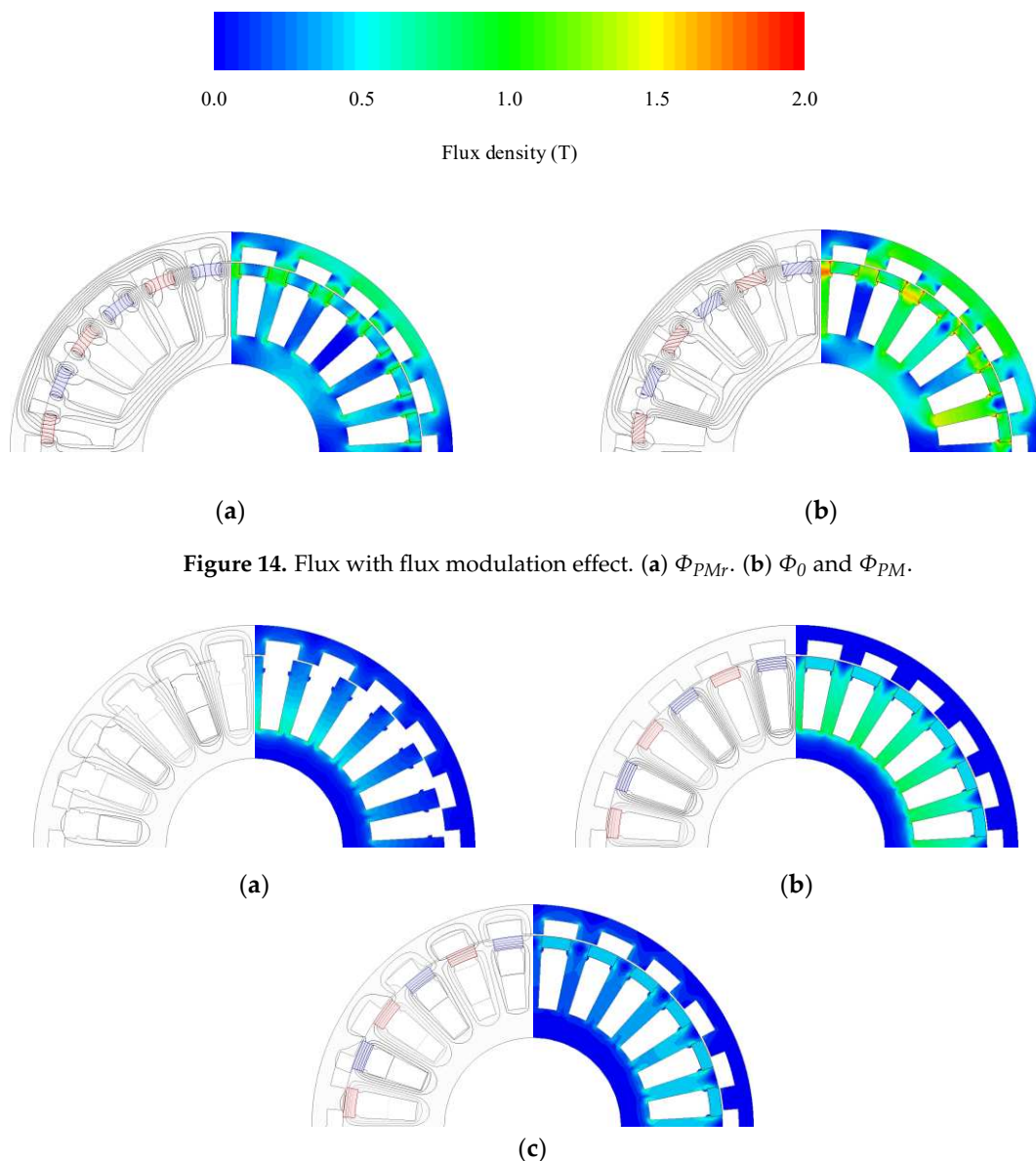


**(a)**  **(b)**

**Figure 14.** Flux with flux modulation effect. (**a**) $\Phi_{PMr}$. (**b**) $\Phi_0$ and $\Phi_{PM}$.



**(a)**  **(b)**

**(c)**

**Figure 15.** Flux with DC-saturation-relieving effect. (**a**) $\Phi_0$. (**b**) $\Phi_{PMt}$. (**c**) $\Phi_0$ and $\Phi_{PMt}$.

### 3.4. Winding Inductance

The open-circuit winding inductance is evaluated in Figure 16. Taking A-phase winding as an example, there are two subphases in A-phase winding as presented in Figure 2, namely, subphases $A_1$ and $A_2$. When the rotor tooth is at the aligned position with subphase $A_1$, subphase $A_2$ must be unaligned with the rotor tooth. Therefore, their inductances can largely mitigate each other when considering the self-inductance of A-phase winding. Therefore, the proposed machine can be approximately regarded as a non-salient pole machine, and an $i_d = 0$ control can be applied to the proposed machine.
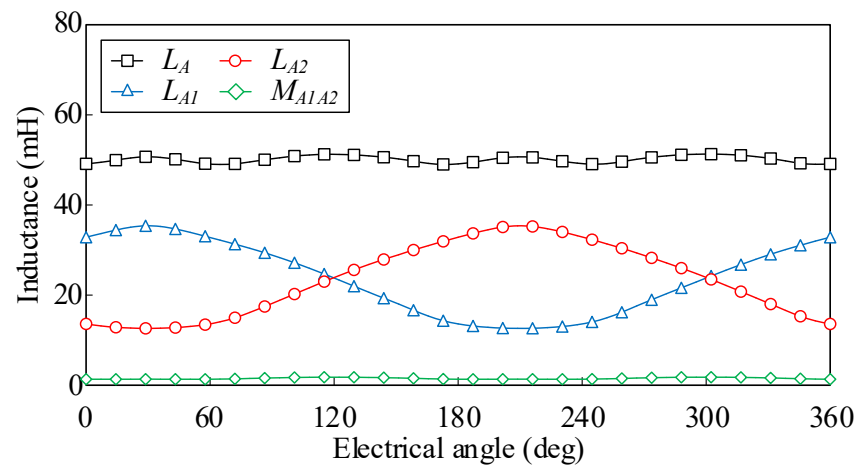


**Figure 16.** Open-circuit winding inductance.

### 3.5. Back EMF

This part gives an analysis of the back EMF in a subphase with different $\alpha_{PM}$ values and the associated EMF contribution of the different excitation sources.

As is presented in Figure 17, $E_{PM}$ is the back EMF contributed by the skewed PM when no current is applied in the armature winding. When $\alpha_{PM}$ is 0, there is no $F_{PMr}$, but $F_{PMt}$ can still produce a little back EMF if the reluctance of the stator yoke is non-negligible, which agrees with the analysis of (4). The higher $\alpha_{PM}$ is, the higher the back EMF is, which agrees with the analytical result in (13).
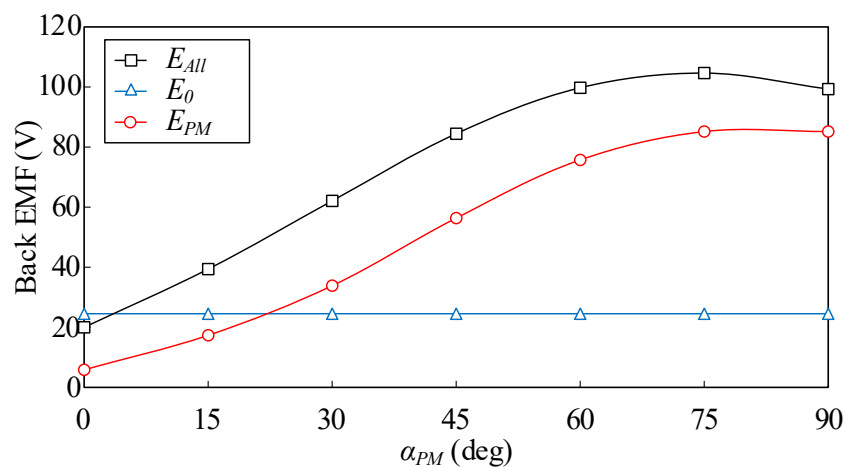


**Figure 17.** Open-circuit back EMF contribution when $\alpha = 63°$.

$E_0$ is the back EMF when $I_0$ is the only excitation source, and, therefore, it is irreverent to $\alpha_{PM}$. $E_{all}$ is the back EMF when both $I_0$ and the skewed PM are used. At the low $\alpha_{PM}$ region, the stator core is over-relieved. Therefore, the growth of $E_{all}$ has a similar tendency

to $E_{PM}$. At the high $\alpha_{PM}$ region, the stator core is under-relieved, which causes the stator core saturation and a drop in the back EMF at the high $\alpha_{PM}$ region.

When $\alpha_{PM} = 60°$, the back EMF is calculated as presented in Figure 18 with both $I_0$ and the skewed PM. $E_{A1}$, $E_{A2}$, and $E_A$ represent the back EMF of subphases A1 and A2, and the total back EMF of phase A, respectively. It can be seen that the even harmonics of subphases A1 and A2 mitigate each other while the odd harmonics are amplified. Therefore, there is no even harmonic in phase A. The total harmonic distortion (THD) of the phase A winding (8.94%) is lower than that of subphases A1 and A2 (17.53%). Therefore, the torque ripple caused by the even harmonics can be eliminated when subphases A1 and A2 are used simultaneously.
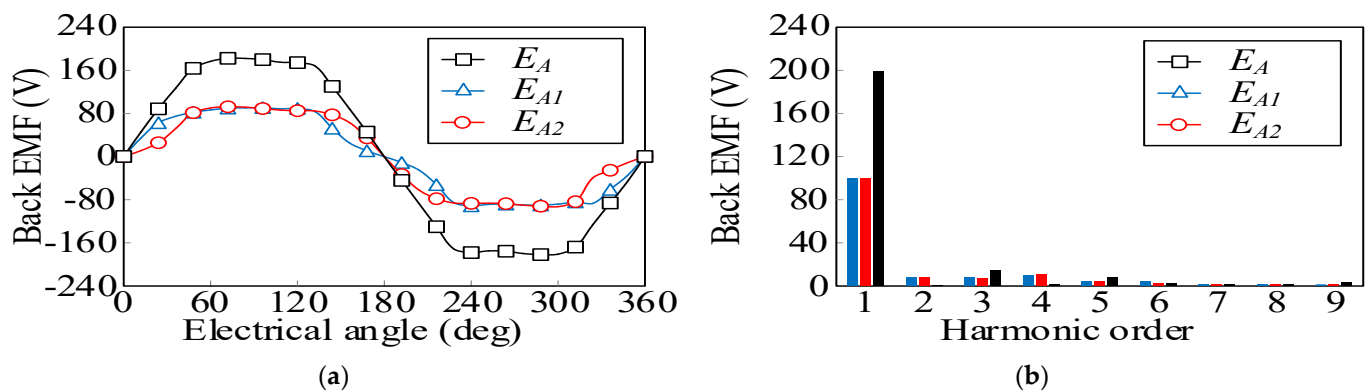


**Figure 18.** Back EMF of subphases A1 and A2 and phase A with $I_0$ and the skewed PM. (**a**) waveform. (**b**) harmonics.

*3.6. Torque Components and Torque Ripple*

The torque productions under different excitation sources are evaluated in Figure 19a, where $T_{PM}$, $T_0$, and $T_{all}$ represent the average torque with the skewed PM, $I_0$, and both the PM and $I_0$. The torque production is in direct proportion to the back EMF if saturation is not considered. Therefore, the tendency of the torque is similar to that of back EMF shown in Figure 17. However, compared with the no-load condition, the introduction of the AC component in the armature current causes easier saturation in the stator core, which requires a higher $F_{PMt}$ to relieve the core saturation. Therefore, although the maximum back EMF is obtained at an $\alpha_{PM}$ of roughly 75°, the maximum torque is achieved at an $\alpha_{PM}$ of approximately 60°.
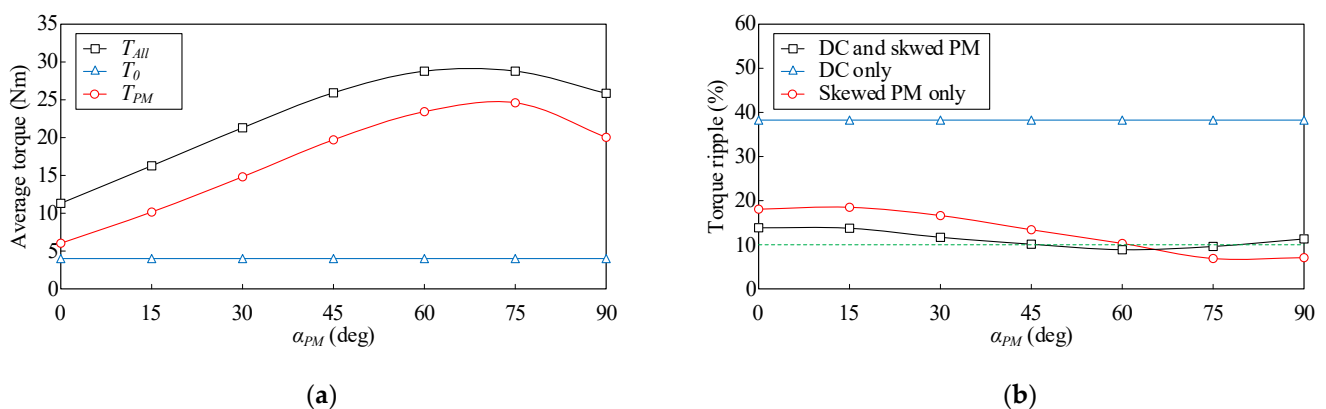


**Figure 19.** Torque production with different excitation sources. (**a**) average torque. (**b**) torque ripple.

The torque ripple under different excitation sources is presented in Figure 19b. There is a large torque ripple when the skewed PM is removed, which is due to two reasons. One is that the lack of $F_{PMt}$, the purpose of which is to demagnetize the stator core, leads to the

working range of the local flux density lying in the nonlinear region of the BH curve, which causes a high torque ripple. Another reason is the absence of the torque contribution from $F_{PMr}$. The torque contributed by $F_{PMr}$ is in direct proportion to the amplitude of $F_{PMr}$ if the core saturation is neglected. When skewed PM and DC current are used simultaneously, the torque ripple is largely reduced compared with that of the machine with the skewed PM. When $\alpha_{PM}$ is from 0 to 60 deg, the torque ripple is reduced as $\alpha_{PM}$ increases. This is due to the rise of $\alpha_{PM}$ bringing higher $F_{PMr}$, which results in a higher torque contribution from $F_{PMr}$. However, at the high $\alpha_{PM}$ region, FPMt is not strong enough to relieve the core saturation caused by the DC current. Therefore, the torque ripple is even higher when $\alpha_{PM}$ exceeds 60 deg.

### 3.7. Core Loss and Efficiency

This part gives an analysis of the core loss and efficiency of the proposed machine. the PM magnetization direction ($\alpha_{PM}$) is set to 60 deg, in consideration of the tradeoff between the torque production and voltage regulation rate (VRR). The current angle ($\beta$) is set to 90 deg, which means an $i_d = 0$ control is adopted. The core loss and efficiency under different zero-sequence current angles ($\alpha$) are evaluated in Figure 20. The current density is set to 6 A/mm$^2$, and therefore the copper loss is a constant in this part.
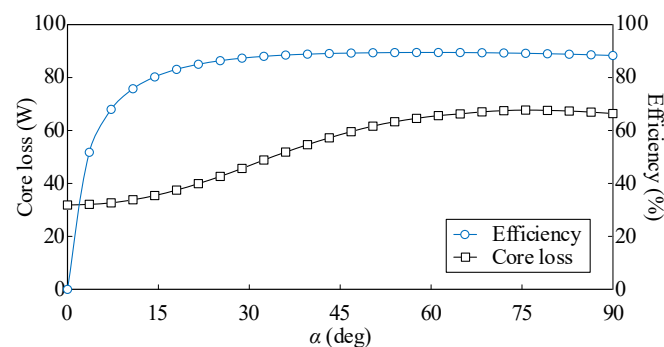


**Figure 20.** Core loss and efficiency under different $\alpha$.

When $\alpha$ is set to 0 deg, there is no AC component in the armature current, and therefore no electromagnetic torque can be generated. Consequently, the efficiency is zero when $\alpha$ is set to 0 deg. In the low $\alpha$ region, with the increase in the AC component in the armature current, the torque and associated efficiency are increased, in spite of the rise in the core loss. The efficiency is almost unchanged in the high $\alpha$ region, which reaches roughly 90%.

The core loss and efficiency under various speed are presented in Figure 21, where $\alpha$ is set to 63 deg. It can be predicted that high efficiency can be achieved, and it is almost unchanged when the speed is above 600 rpm.
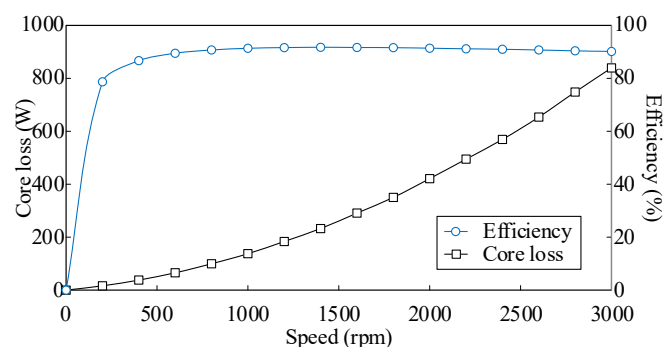


**Figure 21.** Efficiency under different speed.

## 4. Conclusions

In this paper, a novel HRM with the skewed PM and the zero-sequence current excitation is proposed. The key novelty is that the zero-sequence current is introduced with the skewed PM for higher torque production, better VRR and lower copper loss. With the air gap flux modulation effect, enhanced torque production can be achieved by $F_{PMt}$, while with the relieving-DC-saturation effect, VRR expansion can be achieved by $F_{PMr}$.

It is recommended that the magnetization direction ($\alpha_{PM}$) be designed as $60°$ in consideration of the trade-off between torque production and VRR. The torque production is improved by 11.3%, and the VRR is enlarged by 0.306 when the HRM with the skewed PM ($\alpha_{PM} = 60°$) is compared with the traditional design having only radial PM component ($\alpha_{PM} = 90°$). Compared with traditional tangential magnetized PM ($\alpha_{PM} = 0°$), the VRR of HRM with the skewed PM is lower by 0.914, although the average torque is 1.54 times higher than that of its traditional counterpart. Therefore, the proposed HRM topology proves to be a potential solution for electric vehicle propulsion.

## References

1. Zhu, Z.Q.; Cai, S. Hybrid excited permanent magnet machines for electric and hybrid electric vehicles. *China Electrotech. Soc. Trans. Electr. Mach. Syst.* **2019**, *3*, 233–247. [CrossRef]
2. Sun, X.; Shi, Z.; Lei, G.; Guo, Y.; Zhu, J. Analysis and Design Optimization of a Permanent Magnet Synchronous Motor for a Campus Patrol Electric Vehicle. *IEEE Trans. Veh. Technol.* **2019**, *68*, 10535–10544. [CrossRef]
3. Wang, Q.; Niu, S.; Luo, X. A Novel Hybrid Dual-PM Machine Excited by AC With DC Bias for Electric Vehicle Propulsion. *IEEE Trans. Ind. Electron.* **2017**, *64*, 6908–6919. [CrossRef]
4. Trancho, E.; Ibarra, E.; Arias, A.; Kortabarria, I.; Jurgens, J.; Marengo, L.; Fricasse, A.; Gragger, J.V. PM-Assisted Synchronous Reluctance Machine Flux Weakening Control for EV and HEV Applications. *IEEE Trans. Ind. Electron.* **2017**, *65*, 2986–2995. [CrossRef]
5. Jia, S.; Qu, R.; Kong, W.; Li, D.; Li, J.; Yu, Z.; Fang, H. Hybrid Excitation Stator PM Vernier Machines with Novel DC-Biased Sinusoidal Armature Current. *IEEE Trans. Ind. Appl.* **2017**, *54*, 1339–1348. [CrossRef]
6. Wang, Q.; Niu, S. Overview of flux-controllable machines: Electrically excited machines, hybrid excited machines and memory machines. *Renew. Sust. Energ. Rev.* **2017**, *68*, 475–491. [CrossRef]
7. Ahn, J.-W.; Lukman, G.F. Switched reluctance motor: Research trends and overview. *CES Trans. Electr. Mach. Syst.* **2018**, *2*, 339–347. [CrossRef]
8. Zhu, Z.Q.; Cai, S. Overview of hybrid excited machines for electric vehicles. In Proceedings of the 2019 Fourteenth International Conference on Ecological Vehicles and Renewable Energies (EVER), Monte-Carlo, Monaco, 8–10 May 2019; pp. 1–14.
9. Fahimi, B.; Emadi, A.; Sepe, R. A Switched Reluctance Machine-Based Starter/Alternator for More Electric Cars. *IEEE Trans. Energy Convers.* **2004**, *19*, 116–124. [CrossRef]
10. Cheng, M.; Hua, W.; Zhang, J.; Zhao, W. Overview of Stator-Permanent Magnet Brushless Machines. *IEEE Trans. Ind. Electron.* **2011**, *58*, 5087–5101. [CrossRef]
11. Chau, K.T.; Chan, C.C.; Liu, C. Overview of Permanent-Magnet Brushless Drives for Electric and Hybrid Electric Vehicles. *IEEE Trans. Ind. Electron.* **2008**, *55*, 2246–2257. [CrossRef]
12. Liang, X.; Li, G.-J.; Ojeda, J.; Gabsi, M.; Ren, Z. Comparative Study of Classical and Mutually Coupled Switched Reluctance Motors Using Multiphysics Finite-Element Modeling. *IEEE Trans. Ind. Electron.* **2013**, *61*, 5066–5074. [CrossRef]
13. Jarvis, R. Davidson's locomotive: How did he do it? *Eng. Sci. Educ. J.* **1996**, *5*, 281–288. [CrossRef]

14. Zhao, X.; Niu, S.; Fu, W. Design of a Novel Parallel-Hybrid-Excited Dual-PM Machine Based on Armature Harmonics Diversity for Electric Vehicle Propulsion. *IEEE Trans. Ind. Electron.* **2018**, *66*, 4209–4219. [CrossRef]

15. Wang, Y.; Fu, W.N.; Niu, S. A Novel Structure of Dual-Stator Hybrid Excitation Synchronous Motor. *IEEE Trans. Appl. Supercond.* **2016**, *26*, 1–5. [CrossRef]

16. Zhao, X.; Niu, S. Design of a Novel Parallel-Hybrid-Excited Vernier Reluctance Machine with Improved Utilization of Redundant Winding Harmonics. *IEEE Trans. Ind. Electron.* **2018**, *65*, 9056–9067. [CrossRef]

17. Ullah, S.; McDonald, S.P.; Martin, R.; Benarous, M.; Atkinson, G.J. A Permanent Magnet Assist, Segmented Rotor, Switched Reluctance Drive for Fault Tolerant Aerospace Applications. *IEEE Trans. Ind. Appl.* **2019**, *55*, 298–305. [CrossRef]

18. Zheng, M.; Zhu, Z.Q.; Cai, S.; Li, H.Y.; Liu, Y. Influence of Magnetic Saturation and Rotor Eccentricity on Back EMF of Novel Hybrid-Excited Stator Slot Opening Permanent Magnet Machine. *IEEE Trans. Magn.* **2018**, *54*, 1–5.

19. Ding, W.; Yang, S.; Hu, Y.; Li, S.; Wang, T.; Yin, Z. Design Consideration and Evaluation of a 12/8 High-Torque Modular-Stator Hybrid Excitation Switched Reluctance Machine for EV Applications. *IEEE Trans. Ind. Electron.* **2017**, *64*, 9221–9232. [CrossRef]

20. Zhao, X.; Niu, S.; Fu, W. Sensitivity Analysis and Design Optimization of a New Hybrid-Excited Dual-PM Generator with Relieving-DC-Saturation Structure for Stand-Alone Wind Power Generation. *IEEE Trans. Magn.* **2019**, *56*, 1–5. [CrossRef]

21. Afinowi, I.A.A.; Zhu, Z.Q.; Guan, Y.; Mipo, J.C.; Farah, P. Hybrid-Excited Doubly Salient Synchronous Machine with Permanent Magnets Between Adjacent Salient Stator Poles. *IEEE Trans. Magn.* **2015**, *51*, 1–9. [CrossRef]

22. Mao, Y.; Niu, S.; Wang, Q. Design and optimization of a slot-PM-assisted doubly-salient machine based on saturation assuaging. *Chin. J. Electr. Eng.* **2021**, *7*, 65–72. [CrossRef]

23. Jiang, J.; Zhang, X.; Niu, S.; Zhao, X. Novel Doubly-fed Doubly-salient Machine with DC-saturation-relieving Structure for Wind Power Generation. *IET Renew. Power Gener.* **2021**, *15*, 2042–2051. [CrossRef]

24. Zhao, X.; Niu, S.; Zhang, X.; Fu, W. Flux-Modulated Relieving-DC-Saturation Hybrid Reluctance Machine with Synthetic Slot-PM Excitation for Electric Vehicle In-Wheel Propulsion. *IEEE Trans. Ind. Electron.* **2020**, *68*, 6075–6086. [CrossRef]

25. Wang, S.; Niu, S.; Zhao, X.; Fu, W. Novel DC-Saturation-Relieving Hybrid Reluctance Machine with Skewed Permanent Magnets for Electric Vehicle Propulsion. *IEEE Trans. Magn.* **2021**, *58*, 1–6. [CrossRef]

26. Jia, S.; Yan, K.; Liang, D.; Zhu, Z.; Liu, J. Two-Phase DC-Biased Vernier Reluctance Machines. *IEEE Trans. Magn.* **2020**, *57*, 1–5. [CrossRef]

27. Cao, R.; Mi, C.; Cheng, M. Quantitative Comparison of Flux-Switching Permanent-Magnet Motors with Interior Permanent Magnet Motor for EV, HEV, and PHEV Applications. *IEEE Trans. Magn.* **2012**, *48*, 2374–2384. [CrossRef]

28. Zhao, W.; Cheng, M.; Hua, W.; Jia, H.; Cao, R. Back-EMF Harmonic Analysis and Fault-Tolerant Control of Flux-Switching Permanent-Magnet Machine with Redundancy. *IEEE Trans. Ind. Electron.* **2010**, *58*, 1926–1935. [CrossRef]

29. Kolondzovski, Z.; Arkkio, A.; Larjola, J.; Sallinen, P. Power Limits of High-Speed Permanent-Magnet Electrical Machines for Compressor Applications. *IEEE Trans. Energy Convers.* **2010**, *26*, 73–82. [CrossRef]

30. Zhu, Z.Q.; Hua, H.; Wu, D.; Shi, J.T.; Wu, Z.Z. Comparative Study of Partitioned Stator Machines with Different PM Excitation Stators. *IEEE Trans. Ind. Appl.* **2015**, *52*, 199–208. [CrossRef]

31. Zhao, X.; Niu, S.; Fu, W. Torque Component Quantification and Design Guideline for Dual Permanent Magnet Vernier Machine. *IEEE Trans. Magn.* **2019**, *55*, 1–5. [CrossRef]